4 A Solid-State Theoretical Approach to the Optical Properties of Photonic Crystals

K. Busch[1], F. Hagmann[1], D. Hermann[1], S.F. Mingaleev[1,2], and M. Schillinger[2]

[1] Institut für Theorie der Kondensierten Materie, Universität Karlsruhe, 76128 Karlsruhe, Germany
[2] Bogolyubov Institute for Theoretical Physics, 03143 Kiev, Ukraine

Abstract. In this chapter, we outline an efficient approach to the calculation of the optical properties of Photonic Crystals. It is based on solid state theoretical concepts and exploits the conceptual similarity between electron waves propagation in electronic crystals and electromagnetic waves propagation in Photonic Crystals. Based on photonic bandstructure calculations for infinitely extended and perfectly periodic systems, we show how defect structures can be described through an expansion of the electromagnetic field into optimally localized photonic Wannier functions which have encoded in themselves all the information of the underlying Photonic Crystals. This Wannier function approach is supplemented by a multipole expansion method which is well-suited for finite-sized and disordered structures. To illustrate the workings and efficiency of both approaches, we consider several defect structures for TM-polarized radiation in two-dimensional Photonic Crystals.

4.1 Introduction

The invention of the laser turned Optics into Photonics: This novel light source allows one to generate electromagnetic fields with previously unattainable energy densities and temporal as well as spatial coherences. As a result, researchers have embarked on a quest to exploit these properties through perfecting existing and creating novel optical materials with tailor made properties. A particular prominent example is the development of low-loss optical fibers which form the backbone of today's long-haul telecommunication systems [4.1]. With the recent advances in micro-fabrication technologies, another degree of freedom has been added to the flexibility in designing photonic systems: Microstructuring dielectric materials allows one to obtain control over the flow of light on lengths scales of the wavelength of light itself. For instance, the design of high-quality ridge waveguiding structures has facilitated the realization of functional elements for integrated optics such as beamsplitters and Mach-Zehnder interferometers [4.2].

The past two decades have witnessed a strongly increased interest in a novel class of micro-structured optical materials. Photonic Crystals (PCs) consist of a micro-fabricated array of dielectric materials in two or three spatial dimensions. A carefully engineered combination of microscopic scat-

K. Busch, F. Hagmann, D. Hermann, S.F. Mingaleev, and M. Schillinger, A Solid-State Theoretical Approach, Lect. Notes Phys. **642**, 55–74 (2004)
http://www.springerlink.com/

tering resonances from individual elements of the periodic array and Bragg scattering from the corresponding lattice leads to the formation of a photonic bandstructure. In particular, the flexibility in material composition, lattice periodicity, symmetry, and topology of PCs allows one to tailor the photonic dispersion relations to almost any need. The most dramatic modification of the photonic dispersion in these systems occurs when suitably engineered PCs exhibit frequency ranges over which the light propagation is forbidden irrespective of direction [4.3, 4.4]. The existence of these so-called complete Photonic Band Gaps (PBGs) allows one to eliminate the problem of light leakage from sharply bent optical fibers and ridge waveguides. Indeed, using a PC with a complete PBG as a background material and embedding into such a PC a circuit of properly engineered waveguiding channels permits to create an optical micro-circuit inside a perfect optical insulator, i.e. an optical analogue of the customary electronic micro-circuit. In addition, the absence of photon states for frequencies in a complete PBG allows one to suppress the emission of optically active materials embedded in PCs. Furthermore, the multi-branch nature of the photonic bandstructure and low group velocities associated with flat bands near a photonic band edge may be utilized to realize phase-matching for nonlinear optical processes and to enhance the interaction between electromagnetic waves and nonlinear and/or optically active material.

These prospects have triggered enormous experimental activities aimed at the fabrication of two-dimensional (2D) as well as three-dimensional (3D) PC structures for telecommunication applications with PBGs in the near infrared frequency range. Considering that the first Bragg resonance occurs when the lattice constant equals half the wavelength of light, fabrication of PCs with bandgaps in the near IR requires substantial technological resources. For 2D PCs, advanced planar microstructuring techniques borrowed from semiconductor technology can greatly simplify the fabrication process and high-quality PCs with embedded defects and waveguides have been fabricated in various material systems such as semiconductors [4.5–4.10], polymers [4.11,4.12], and glasses [4.13,4.14]. In these structures, light experiences PBG effects in the plane of propagation, while the confinement in the third direction is achieved through index guiding. This suggests that fabricational imperfections in bulk 2D PCs as well deliberately embedding defect structures such as cavities and waveguide bends into 2D PCs will inevitably lead to radiation losses into the third dimension. Therefore, it is still an open question as to whether devices with acceptable radiation losses can be designed and realized in 2D PCs. However, radiation losses can be avoided altogether if light is guided within the comlete PBG of 3D PCs and, therefore, the past years have seen substantial efforts towards the manufacturing of suitable 3D PCs. These structures include layer-by-layer structures [4.15, 4.16], inverse opals [4.17–4.19] as well as the fabrication of templates via laser holography [4.20, 4.21] and two-photon polymerization (sometimes also referred to as stereo-lithography) [4.22–4.24].

Given this tremendous flexibility in the fabrication of PCs (and the cost associated with most of the fabrication techniques), it is clear that modeling of the linear, nonlinear and quantum optical properties of PCs is a crucial element of PC research. In this manuscript, we would like to outline how the far-reaching analogies of electron wave propagation in crystalline solids and electromagnetic wave propagation in PCs can be utilized to obtain a theoretical framework for the quantitative description of light propagation in PCs. In Sect. 4.2, we describe an efficient method for obtaining the photonic bandstructure which is based on a Multi-Grid technique. The results of photonic bandstructure computations are the basis for the description of defect structures such as cavities and waveguides using a Wannier function approach (Sect. 4.3). As an example, we illustrate the design of a near optimal PC waveguide bend. Finally, in Sect. 4.4, we utilize this bend design and a multipole expansion technique to construct a PC beamsplitter within a finite-sized PC and discuss the role of fabricational tolerances on the performance of the device.

4.2 Photonic Bandstructure Computation

Photonic bandstructure computations determine the dispersion relation of infinitely extended defect-free PCs. In addition, they allow one to design PCs that exhibit PBGs and to accurately interpret measurements on PC samples. As a consequence, photonic bandstructure calculations represent an important predictive as well as interpretative basis for PC research and, therefore, lie at the heart of theoretical investigations of PCs. More specifically, the goal of photonic bandstructure computations is to find the eigenfrequencies and associated eigenmodes of the wave equation for the perfect PC, i.e., for an infinitely extended periodic array of dielectric material. For the simplicity of presentation we restrict ourselves in the remainder of this manuscript to the case of TM-polarized radiation propagating in the plane of periodicity (x, y)-plane of 2D PCs. In this case, the wave equation in the frequency domain (harmonic time dependence) for the z-component of the electric field reads

$$\frac{1}{\epsilon_{\mathrm{p}}(\boldsymbol{r})}\left(\partial_x^2+\partial_y^2\right)E(\boldsymbol{r})+\frac{\omega^2}{c^2}E(\boldsymbol{r})=0. \tag{4.1}$$

Here c denotes the vacuum speed of light and $\boldsymbol{r} = (x, y)$ denotes a two-dimensional position vector. The dielectric constant $\epsilon_{\mathrm{p}}(\boldsymbol{r}) \equiv \epsilon_{\mathrm{p}}(\boldsymbol{r} + \boldsymbol{R})$ is periodic with respect to the set $\mathcal{R} = \{n_1\boldsymbol{a}_1 + n_2\boldsymbol{a}_2; (n_1, n_2) \in \mathcal{Z}^2\}$ of lattice vectors $\boldsymbol{R}$ generated by the primitive translations $\boldsymbol{a}_i,\ i = 1, 2$ that describe the structure of the PC. Equation (4.1) represents a differential equation with periodic coefficients and, therefore, its solutions obey the Bloch-Floquet theorem

$$E_{\boldsymbol{k}}(\boldsymbol{r}+\boldsymbol{a}_i)=e^{i\boldsymbol{k}\boldsymbol{a}_i}\,E_{\boldsymbol{k}}(\boldsymbol{r}), \tag{4.2}$$

where $i = 1, 2$. The wave vector $\boldsymbol{k} \in 1.\mathrm{BZ}$ that labels the solution is a vector of the first Brillouin zone (BZ) known as the crystal momentum. As a result of this reduced zone scheme, the photonic bandstructure acquires a multi-branch nature that is associated with the backfolding of the dispersion relation into the 1. BZ. This introduces a discrete index n, the so-called band index, that enumarates the distinct eigenfrequencies and eigenfunctions at the same wave vector $\boldsymbol{k}$.

The photonic dispersion relation $\omega_n(\boldsymbol{k})$ gives rise to a photonic Density of States (DOS), which plays a fundamental role for the understanding of the quantum optical properties of active material embedded in PCs [4.25]. The photonic DOS, $N(\omega)$, is defined by "counting" all allowed states with a given frequency ω

$$N(\omega) = \sum_n \int_{1.\mathrm{BZ}} d^2k \; \delta(\omega - \omega_n(\boldsymbol{k})). \tag{4.3}$$

Other physical quantities such as group velocities $\boldsymbol{v}_n(\boldsymbol{k}) = \nabla_{\boldsymbol{k}}\omega_n(\boldsymbol{k})$ can be calculated through adaption of various techniques known from electron bandstructure theory. For details, we refer to [4.26] and [4.27].

A straightforward way of solving (4.1) is to expand all the periodic functions into a Fourier series over the reciprocal lattice $\mathcal{G}$, thereby transforming the differential equation into an infinite matrix eigenvalue problem, which may be suitably truncated and solved numerically. Details of this plane wave method (PWM) for isotropic systems can be found, for instance, in [4.26,4.28] and for anisotropic systems in [4.29]. While the PWM provides a straightforward approach to computing the bandstructure of PCs, it also exhibits a number of shortcomings such as slow convergence associated with the truncation of Fourier series in the presence of discontinuous changes in the dielectric constants. In particular, this slow convergence makes the accurate calculation of Bloch functions a formidable and resource-consuming task. Therefore, we have recently developed an efficient real space approach to computing photonic bandstructures [4.27]. Within this approach, the wave equation, (4.1), is discretized in a single unit cell in real space (defined through the set of space points $\boldsymbol{r} = r_1\boldsymbol{a}_1 + r_2\boldsymbol{a}_2$ with $r_1, r_2 \in [-1/2, 1/2]$), leading to a sparse matrix problem. The Bloch-Floquet theorem, (4.2), provides the boundary condition for the elliptic partial differential equation (4.1). In addition, the eigenvalue is treated as an additional unknown for which the normalization of the Bloch functions provides the additional equation needed for obtaining a well-defined problem. The solution of this algebraic problem is obtained by employing Multi-Grid (MG) methods which guarantee an efficient solution by taking full advantage of the smoothness of the photonic Bloch functions [4.27,4.30] (see also the chapter of G. Wittum in this volume). Even for the case of a naive finite difference discretization, the MG-approach easily outperforms the PWM and leads to a substantial reduction in CPU time. For instance, in the present case of 2D systems for which the Bloch functions are required we save one order of magnitude in CPU time as compared

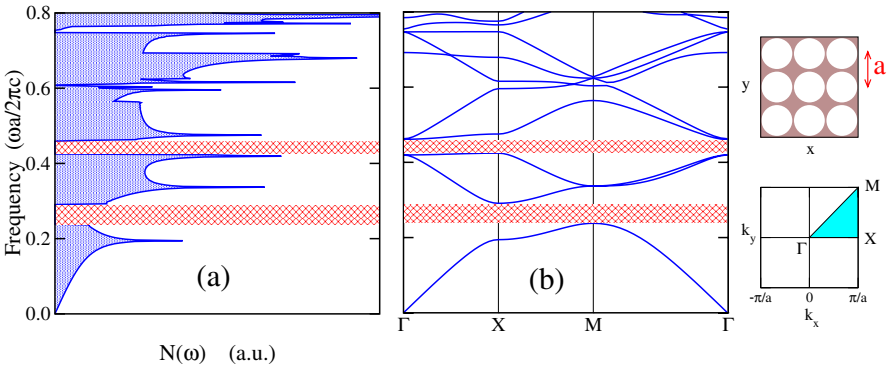

Fig. 4.1. Density of States (a) and photonic band structure (b) for TM-polarized radiation in a square lattice (lattice constant a) of cylindrical air pores of radius $R_{\text{pore}} = 0.475a$ in dielectric with $\varepsilon = 12$ (silicon). This PC exhibits a large fundamental gap extending from $\omega = 0.238 \times 2\pi c/a$ to $\omega = 0.291 \times 2\pi c/a$. A higher order band gap extends from $\omega = 0.425 \times 2\pi c/a$ to $\omega = 0.464 \times 2\pi c/a$.

to PWM. Additional refinements such as a finite element discretization will further increase the efficiency of the MG-approach.

In Fig. 4.1(b), we show the bandstructure for TM-polarized radiation in a 2D PC consisting of a square lattice (lattice constant a) of cylindrical air pores (radius $r_{\text{pore}} = 0.475a$) in a silicon matrix ($\varepsilon_{\text{p}} = 12$). This structure exhibits two 2D PBGs. The larger, fundamental bandgap (20% of the midgap frequency) extends between $\omega = 0.238 \times 2\pi c/a$ to $\omega = 0.291 \times 2\pi c/a$ and the smaller, higher order bandgap (8% of the midgap frequency) extends from $\omega = 0.425 \times 2\pi c/a$ to $\omega = 0.464 \times 2\pi c/a$. Furthermore, in Fig. 4.1(a) we depict the DOS for our model system, where the photonic band gaps are manifest as regions of vanishing DOS. Characteristic for 2D systems is the linear behavior for small frequencies as well as the logarithmic singularities, the so-called van Hove singularities, associated with vanishing group velocities for certain frequencies inside the bands (compare with Fig. 4.1(a)).

4.3 Defect Structures in Photonic Crystals

To date, the overwhelming majority of theoretical investigations of cavities and waveguiding in PCs has been carried out using Finite-Difference Time-Domain (FDTD) and/or Finite-Element (FE) techniques. However, applying general purpose methodologies such as FDTD or FE methods to defect structures in PCs largely disregards information about the underlying PC structure which is readily available from photonic bandstructure computation. As a result, only relatively small systems can be investigated and the physical insight remains limited.

4.3.1 Maximally Localized Photonic Wannier Functions

A more natural description of localized defect modes in PCs consists in an expansion of the electromagnetic field into a set of localized basis functions which have encoded into them all the information of the underlying PC. Therefore, the most natural basis functions for the description of defect structures in PCs are the so-called photonic Wannier functions, $W_{n\boldsymbol{R}}(\boldsymbol{r})$, which are formally defined through a lattice Fourier transform

$$W_{n\boldsymbol{R}}(\boldsymbol{r}) = \frac{V_{\mathrm{WSC}}}{(2\pi)^2} \int_{\mathrm{BZ}} d^2\boldsymbol{k}\, e^{-i\boldsymbol{k}\boldsymbol{R}}\, E_{n\boldsymbol{k}}(\boldsymbol{r}) \tag{4.4}$$

of the extended Bloch functions, $E_{n\boldsymbol{k}}(\boldsymbol{r})$. The above definition associates the photonic Wannier function $W_{n\boldsymbol{R}}(\boldsymbol{r})$ with the frequency range covered by band n, and centers it around the corresponding lattice site $\boldsymbol{R}$. In addition, the completeness and orthogonality of the Bloch functions translate directly into corresponding properties of the photonic Wannier functions. Computing the Wannier functions directly from the output of photonic bandstructure programs via (4.4) leads to functions with poor localization properties and erratic behavior (see, for instance, Fig. 2 in [4.31]). These problems originate from an indeterminacy of the global phases of the Bloch functions. It is straightforward to show that for a group of N_{W} bands there exists, for every wave vector $\boldsymbol{k}$, a free unitary transformation between the bands which leaves the orthogonality relation of Wannier functions unchanged. A solution to this unfortunate situation is provided by recent advances in electronic bandstructure theory. Marzari and Vanderbilt [4.32] have outlined an efficient scheme for the computation of maximally localized Wannier functions by determining numerically a unitary transformation between the bands that minimizes an appropriate spread functional $\mathcal{F}$

$$\mathcal{F} = \sum_{n=1}^{N_{\mathrm{W}}} \left[\langle n\boldsymbol{0}|\, r^2\, |n\boldsymbol{0}\rangle - (\langle n\boldsymbol{0}|\, \boldsymbol{r}\, |n\boldsymbol{0}\rangle)^2 \right] = \mathrm{Min}\ . \tag{4.5}$$

Here we have introduced a shorthand notation for matrix elements according to

$$\langle n\boldsymbol{R}|\, f(\boldsymbol{r})\, |n'\boldsymbol{R}'\rangle = \int_{\mathbf{R}^2} d^2r\, W^*_{n\boldsymbol{R}}(\boldsymbol{r})\, f(\boldsymbol{r})\, \varepsilon_{\mathrm{p}}(\boldsymbol{r})\, W_{n'\boldsymbol{R}'}(\boldsymbol{r})\ , \tag{4.6}$$

for any function $f(\boldsymbol{r})$. For instance, the orthonormality of the Wannier functions in this notation read as

$$\langle n\boldsymbol{R}|\, |n'\boldsymbol{R}'\rangle = \int_{\mathbf{R}^2} d^2r\, W^*_{n\boldsymbol{R}}(\boldsymbol{r})\, \varepsilon_{\mathrm{p}}(\boldsymbol{r})\, W_{n'\boldsymbol{R}'}(\boldsymbol{r}) = \delta_{nm}\delta_{\boldsymbol{R}\boldsymbol{R}'}\ , \tag{4.7}$$

The field distributions of the optimized Wannier functions belonging to the six most relevant bands of our model system are depicted in Fig. 4.2 (see

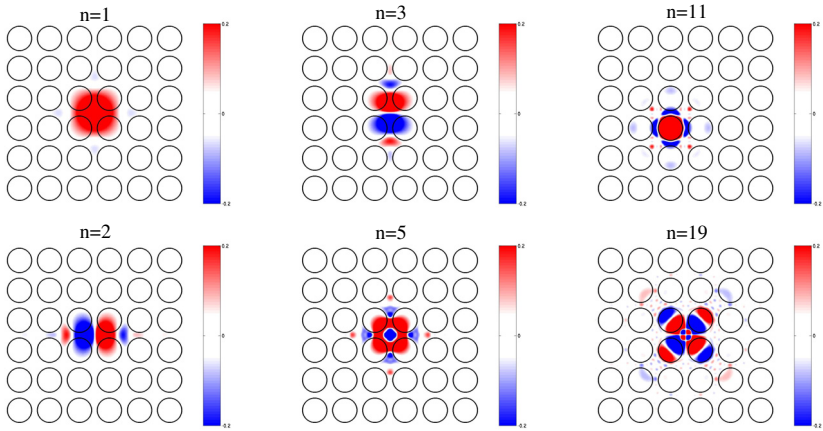

Fig. 4.2. Photonic Wannier functions, $W_{n\mathbf{0}}(\boldsymbol{r})$, for the six bands that are most relevant for the description of the localized defect mode shown in Fig. 4.3(a). These optimally localized Wannier functions have been obtained by minimizing the corresponding spread functional, (4.5). Note, that in contrast to the other bands, the Wannier center of the eleventh band is located at the center of the air pore. The parameters of the underlying PC are the same as those in Fig. 4.1.

also the discussion in Sect. 4.3.3). Their localization properties as well as the symmetries of the underlying PC structure are clearly visible. It should be noted that the Wannier centers of all calculated bands (except of the eleventh band) are located halfway between the air pores, i.e. inside the dielectric (see [4.32] for more details on the Wannier centers). In addition, we would like to point out that instead of working with the electric field [4.33, 4.31], (4.1), one may equally well construct photonic Wannier functions for the magnetic field, as recently demonstrated by Whittaker and Croucher [4.34].

4.3.2 Defect Structures via Wannier Functions

The description of defect structures embedded in PCs starts with the corresponding wave equation in the frequency domain

$$\nabla^2 E(\boldsymbol{r}) + \left(\frac{\omega}{c}\right)^2 \left(\varepsilon_{\mathrm{p}}(\boldsymbol{r}) + \delta\varepsilon(\boldsymbol{r})\right) E(\boldsymbol{r}) = 0 \,. \tag{4.8}$$

Here, we have decomposed the dielectric function into the periodic part, $\varepsilon_{\mathrm{p}}(\boldsymbol{r})$, and the contribution, $\delta\varepsilon(\boldsymbol{r})$, that describes the defect structures. Within the Wannier function approach, we expand the electromagnetic field according to

$$E(\boldsymbol{r}) = \sum_{n,\boldsymbol{R}} E_{n\boldsymbol{R}}\, W_{n\boldsymbol{R}}(\boldsymbol{r}) \,, \tag{4.9}$$

with unknown amplitudes $E_{n\boldsymbol{R}}$. Inserting this expansion into the wave equation (4.8) and employing the orthonomality relations, (4.7), leads to the basic equation for lattice models of defect structures embedded in PCs

$$\sum_{n',\boldsymbol{R}'} \left\{ \delta_{nn'}\delta_{\boldsymbol{R}\boldsymbol{R}'} + D^{nn'}_{\boldsymbol{R}\boldsymbol{R}'} \right\} E_{n'\boldsymbol{R}'} = \left(\frac{c}{\omega}\right)^2 \sum_{n',\boldsymbol{R}'} A^{nn'}_{\boldsymbol{R}\boldsymbol{R}'} E_{n'\boldsymbol{R}'} \ . \tag{4.10}$$

The matrix $A^{nn'}_{\boldsymbol{R}\boldsymbol{R}'}$ depends only on the Wannier functions of the underlying PC and is defined through

$$A^{nn'}_{\boldsymbol{R}\boldsymbol{R}'} = -\int_{\mathbf{R}^2} d^2\boldsymbol{r} \ \ W^*_{n\boldsymbol{R}}(\boldsymbol{r}) \, \nabla^2 \, W_{n'\boldsymbol{R}'}(\boldsymbol{r}) \ . \tag{4.11}$$

The localization of the Wannier functions in space leads to a very rapid decay of the magnitude of matrix elements with increasing separation $|\boldsymbol{R} - \boldsymbol{R}'|$ between lattice sites, effectively making the matrix $A^{nn'}_{\boldsymbol{R}\boldsymbol{R}'}$ sparse. Furthermore, it may be shown that the matrix $A^{nn'}_{\boldsymbol{R}\boldsymbol{R}'}$ is Hermitian and positive definite. Similarly, once the Wannier functions of the underlying PC are determined, the matrix $D^{nn'}_{\boldsymbol{R}\boldsymbol{R}'}$ depends solely on the overlap of these functions, mediated by the defect structure:

$$D^{nn'}_{\boldsymbol{R}\boldsymbol{R}'} = \int_{\mathbf{R}^2} d^2\boldsymbol{r} \ \ W^*_{n\boldsymbol{R}}(\boldsymbol{r}) \, \delta\varepsilon(\boldsymbol{r}) \, W_{n'\boldsymbol{R}'}(\boldsymbol{r}) \ . \tag{4.12}$$

As a consequence of the localization properties of both the Wannier functions and the defect dielectric function, the Hermitian matrix $D^{nn'}_{\boldsymbol{R}\boldsymbol{R}'}$, too, is sparse. In the case of PCs with inversion symmetry, $\varepsilon_{\mathrm{p}}(\boldsymbol{r}) \equiv \varepsilon_{\mathrm{p}}(-\boldsymbol{r})$, the Wannier functions can be chosen to be real. Accordingly, both matrices, $A^{nn'}_{\boldsymbol{R}\boldsymbol{R}'}$ and $D^{nn'}_{\boldsymbol{R}\boldsymbol{R}'}$ become real symmetric ones.

Depending on the nature of the defect structure, we are interested in (i) frequencies of localized cavity modes, (ii) dispersion relations for straight waveguides, or (iii) transmission and reflection through waveguide bends and other, more complex defect structures. In the following, we consider each of these cases separately.

4.3.3 Localized Cavity Modes

As a first illustration of the Wannier function approach, we consider the case of a simple cavity created by infiltrating a single pore at the defect site $\boldsymbol{R}_{\mathrm{def}}$ with a material with dielectric constant $\varepsilon_{\mathrm{def}}$, as shown in the inset of Fig. 4.3(a). In this case, we directly solve (4.10) as a generalized eigenvalue problem for the cavity frequencies that lie within the PBG, and reconstruct the cavity modes from the corresponding eigenvectors. In Fig. 4.3(a) we compare the frequencies of these cavity modes calculated from (4.10) with corresponding calculations using PWM-based super-cell calculations.

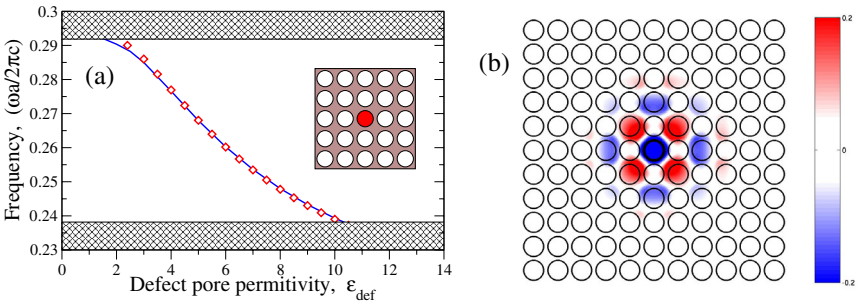

Fig. 4.3. (a) Frequencies of localized cavity modes created by infiltrating a single defect pore with a material with dielectric constant $\varepsilon_{\rm def}$ (see inset). The results of the Wannier function approach (diamonds) using $N_{\rm W} = 10$ Wannier functions per unit cell are in complete agreement with numerically exact results of the super-cell calculations (full line). The parameters of the underlying PC are the same as those in Fig 4.1. **(b)** Electric field distribution for the cavity mode with frequency $\omega = 0.290 \times 2\pi c/a$, created by infiltrating the pore with a polymer with $\varepsilon_{\rm def} = 2.4$.

Upon increasing $\varepsilon_{\rm def}$, a non-degenerate cavity mode with monopole symmetry emerges from the upper edge of the bandgap. The results of the Wannier function approach using the $N_{\rm W} = 10$ most relevant Wannier functions *per unit cell* in (4.10) are in complete agreement with numerically exact results of the super-cell calculations. In Fig. 4.3(b), we depict the corresponding mode

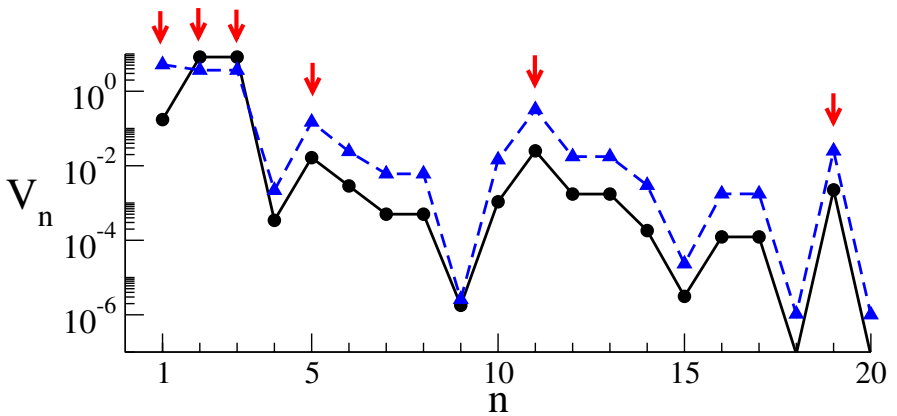

Fig. 4.4. The strength V_n of the individual contributions from the Wannier functions of the lowest 20 bands (index n) to the formation of the cavity modes depicted in Fig. 4.3. The Wannier functions with $V_n \leq 10^{-3}$ may be safely leaved out of account. Arrows indicate the six must relevant Wannier functions depicted in Fig. 4.2. The parameters of the underlying PC are the same as those in Fig. 4.1.

structure for a monopole cavity mode created by infiltration of a polymer with $\varepsilon_{\rm def} = 2.4$ into the pore. The convergence properties of the Wannier function approach should depend on the nature and symmetry properties of the cavity modes under consideration. To discuss this issue in greater detail, it is helpful to define a measure V_n of the strength of the contributions to a cavity mode from the individual Wannier function associated with band n via $V_n = \sum_{\boldsymbol{R}} |E_{n\boldsymbol{R}}|^2$. In Fig. 4.4 we display the dependence of the parameter V_n on the band index n for the cavity modes shown in Fig. 4.3, for two values of the defect dielectric constant, $\varepsilon_{\rm def} = 2.4$ (solid line) and $\varepsilon_{\rm def} = 8$ (dashed line), respectively. In both cases, the most relevant contributions to the cavity modes originate from the Wannier functions belonging to bands $n = 1, 2, 3, 5, 11$, and 19, and all contributions from bands $n > 20$ are negligible. These most relevant Wannier functions for our model system are shown in Fig. 4.2. In fact, fully converged results are obtained when we work with the 10 most relevant Wannier functions per unit cell (for a comparison with numerically exact super-cell calculations see Fig. 4.3(a)).

4.3.4 Dispersion Relations of Waveguides

The efficiency of the Wannier function approach is particularly evident when considering defect clusters consisting of several defect pores. In this case the defect dielectric function, $\delta\varepsilon(\boldsymbol{r})$, can be written as a sum over positions, $\boldsymbol{R}_m$, of the individual defect pores, so that (4.12) reduces to a sum

$$D^{nn'}_{\boldsymbol{R}\boldsymbol{R}'} = \sum_m D(m)^{nn'}_{\boldsymbol{R}-\boldsymbol{R}_m,\boldsymbol{R}'-\boldsymbol{R}_m} \ , \tag{4.13}$$

over the matrix elements $D(m)^{nn'}_{\boldsymbol{R},\boldsymbol{R}'}$ of the individual defects (see discussion in [4.31] for more details). Therefore, for a given underlying PC structure, it becomes possible to build up a database of matrix elements, $D(m)^{nn'}_{\boldsymbol{R},\boldsymbol{R}'}$, for different geometries (radii, shapes) of defect pores, which allow us highly efficient defect computations through simple matrix assembly procedures. This is in strong contrast to *any* other computational technique known to us.

Arguably the most important types of defect clusters in PCs are one or several adjacent straight rows of defects. Properly designed, such defect rows form a PC waveguide which allows the efficient guiding of light for frequencies within a PBG [4.35, 4.36]. Due to the one-dimensional periodicity of such a waveguide, its guided modes, $E^{(p)}(\boldsymbol{r}\,|\,\omega) = \sum_{n,\boldsymbol{R}} E^{(p)}_{n\boldsymbol{R}}(\omega)\, W_{n\boldsymbol{R}}(\boldsymbol{r})$, obey the 1D Bloch-Floquet theorem

$$E^{(p)}_{n\boldsymbol{R}+\boldsymbol{s}_{\rm w}}(\omega) = e^{i\boldsymbol{k}_p(\omega)\boldsymbol{s}_{\rm w}}\, E^{(p)}_{n\boldsymbol{R}}(\omega) \ , \tag{4.14}$$

and thus they can be labeled by a wave vector, $\boldsymbol{k}_p(\omega)$, parallel to the waveguide director, $\boldsymbol{s}_{\rm w}{=}w_1\boldsymbol{a}_1 + w_2\boldsymbol{a}_2$, where $\boldsymbol{a}_1{=}(a, 0)$ and $\boldsymbol{a}_2{=}(0, a)$ are the primitive lattice vectors of the PC, and integers w_1 and w_2 define the direction

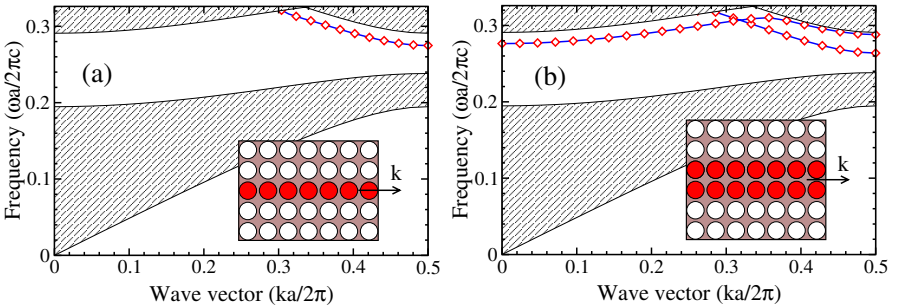

Fig. 4.5. Dispersion relations of the propagating guided mode for PC waveguides consisting of **(a)** one row and **(b)** two rows of defect pores infiltrated with a polymer with $\varepsilon_{\rm def} = 2.4$. The calculations within the Wannier function approach (diamonds), based on (4.10) and (4.14) in which we accounted for the interaction of 5 nearest pores along the waveguide and used 10 most relevant Wannier functions per unit cell, are in complete agreement with the results of supercell calculations (solid lines). The gray areas represent the projected band structure of the underlying model PC (see Fig. 4.1). The red circles in the insets indicate the positions of the infiltrated pores.

of the waveguide (for instance, an x-axis directed W1-waveguide is described through w_1=1 and w_2=0). Commonly, investigations of PC waveguides consist of calculations of the dispersion relations, $\boldsymbol{k}_p(\omega)$, of all the guided modes, which can be obtained by substituting (4.14) into (4.10) as is described in details in [4.31].

To date, investigations of straight PC waveguides have concentrated on the calculation of dispersion relations for *propagating guided modes* with real wave vectors, $k_{\rm p}(\omega)$, only. Such calculations can be accurately carried out also by employing the supercell technique. In Fig. 4.5 we display the dispersion relations for the propagating guided modes of the W1 and W2 waveguides created by infiltrating a polymer into one row and two rows of pores, calculated within the Wannier function approach. The results of these calculations are fully converged and in complete agreement with the results of plane-wave based supercell computations. Similar to the calculations of complex cavity structures, the calculations of waveguide dispersion relations within the Wannier function approach require fairly minimal computational resources in comparison with the supercell technique.

We would like to emphasize that, in contrast to the supercell technique, the Wannier function approach enables us to also obtain the dispersion relations for *evanescent guided modes* with complex wave vectors $k_{\rm p}(\omega)$. Since such modes grow or decay along the waveguide direction, they are largely irrelevant in perfectly periodic straight waveguides. However, they start to play an important role as soon as the perfect periodicity of the waveguide is broken either through imperfections due to fabricational tolerances, or through the deliberate creation of deviations from periodicity such as bends or cou-

pled cavity-waveguide systems for Wavelength Division Multiplexing (WDM) applications. In such cases, these *evanescent* guided modes give rise to light localization effects and determine the non-trivial transmission and reflection properties of PC circuits [4.31, 4.37] as we will discuss below.

4.3.5 Photonic Crystal Circuits

In this section we demonstrate that the Wannier function approach provides an efficient simulation tool for the description of light through PC circuits which allows one to overcome most of the limitations related to FDTD or FE methods. As an illustration, we consider light propagation through two-port PC circuits such as waveguide bends or coupled cavity-waveguide systems. The common feature of these devices is that two semi-infinite straight PC waveguides act as leads that are connected through a finite-sized region of defects. In this case, light propagation through the device at frequency ω is governed by (4.10), which should be truncated (to obtain equal number of equations and unknowns) by prescribing certain values to the expansion coefficients, $E_{n\boldsymbol{R}}$, at some sites inside the waveguiding leads. Since these values determine the amplitudes of the incoming light, it is physically more transparent to express the expansion coefficients $E_{n\boldsymbol{R}}$ within the leads through a superposition of the guided modes $\boldsymbol{\Phi}^{(p)}(\omega)$ with wave vectors $k_{\mathrm{p}}(\omega)$ of the corresponding infinite straight waveguide. In a numerical implementation this is facilitated by replacing the expansion coefficients $E_{n\boldsymbol{R}}$ for all lattice sites $\boldsymbol{R}$ inside each waveguiding lead, W_i, $i = 1, 2$, according to

$$E^{\mathrm{w}_i}_{n\boldsymbol{R}} = \sum_{p=1}^{N} u^{(p)}_{\mathrm{w}_i}(\omega) E^{(p)}_{n\boldsymbol{R}}(\omega) + \sum_{p=N+1}^{2N} d^{(p)}_{\mathrm{w}_i}(\omega) E^{(p)}_{n\boldsymbol{R}}(\omega) \,, \tag{4.15}$$

where $u^{(p)}_{\mathrm{w}_i}$ and $d^{(p)}_{\mathrm{w}_i}$ are amplitudes of the guided modes, and we assume that all $2N$ guided modes are ordered in the following way: $p = 1$ to N are occupied by the propagating guided modes with $\mathrm{Re}[k_{\mathrm{p}}] > 0$ and evanescent guided modes with $\mathrm{Im}[k_{\mathrm{p}}] > 0$, whereas $p = N+1$ to $2N$ are occupied by the propagating guided modes with $\mathrm{Re}[k_{\mathrm{p}}] < 0$ and evanescent guided modes with $\mathrm{Im}[k_{\mathrm{p}}] < 0$. Assuming that the amplitudes, $u^{(p)}_{\mathrm{w}_1}$ and $d^{(p)}_{\mathrm{w}_2}$, of all the propagating (evanescent) guided modes which propagate (decay) in the direction of the device are known (they depend on the purpose of our calculation or on the experimental setup), we can now substitute (4.15) into (4.10) and, solving the resulting system of coupled equations, find the unknown expansion coefficients $E_{n\boldsymbol{R}}$ for the sites $\boldsymbol{R}$ inside the domain of the device (which can be used, e.g., for visualization of the field propagation through the device), and the amplitudes, $u^{(p)}_{\mathrm{w}_2}$ and $d^{(p)}_{\mathrm{w}_1}$ of all *outgoing propagating* and *growing evanescent* guided modes. In [4.31] some of us have demonstrated, by comparison with the FDTD calculations [4.35], that the results of such transmission calculations based on the Wannier function approach are indeed very accurate and

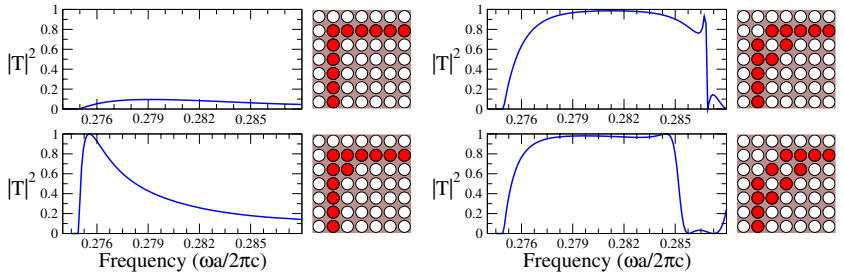

Fig. 4.6. Transmission spectra, $|T(\omega)|^2$, for four different bend geometries embedded in our 2D model PC. The results of the Wannier function approach are obtained with $N_{\mathrm{R}} = 5$, $L = 5$, and the $N_{\mathrm{W}} = 10$ most relevant Wannier functions. The parameters of the underlying PC are the same as those in Fig. 4.1.

agree extremely well with FDTD calculations. Now, in Fig. 4.6, we present the results of Wannier function calculations of the transmission spectra for four different bend geometries with attached single-mode waveguide leads (see Fig. 4.5) that are embedded in our model PC. The improvement of the optimal design (lower right in Fig. 4.6) over the naive bend (upper left in Fig. 4.6) is apparent: For the optimal design we find a wide frequency range of nearly perfect transmission as opposed to maximal 10% transmission in the naive design. In Sect. 4.4, we will utilize this optimized bend design for the construction of a beamsplitter and a discussion of the influence of fabricational tolerances on the performance of the device.

The efficiency of the Wannier function approach for transmission calculations becomes apparent when considering that – once the Wannier functions for the underlying PC have been obtained – the calculation of a single data point in the reflection spectra of Fig. 4.6 reduces to the solution of a single sparse system of some 800 equations, which even on a laptop computer takes only a few seconds. Therefore, the Wannier function approach outlined above will (i) enable a reverse engineering of defect structures with prescribed functionality and (ii) allow detailed studies regarding the robustness of successful designs with respect to fabricational tolerances. Moreover, the Wannier function approach can be straightforwardly applied, with comparable efficiency, to investigations of the transmission spectra through PC circuits made from highly dispersive and/or nonlinear materials. Of paramount importance is the fact that, in contrast to the FDTD or FE methods, the Wannier function approach permits one to accurately and efficiently calculate the complete scattering matrices of PC devices [4.31], allowing us to construct a PC circuit theory in which *individual devices are replaced by simple equivalent scattering matrices* which are assembled by simple scattering matrix multiplication rules to form the scattering matrix of *large-scale circuits* [4.38]. We would like to emphasize that in some sense these scattering matrices can be regarded as the optical analogue of the impedance matrices associated with multi-port devices in microwave technology [4.39].

4.4 Finite Photonic Crystals

The Wannier function approach described above is particularly useful for large systems, and has no restriction in the shape of the elements conforming the system. Extensions of this approach have to include the description of coupling in and out of PCs, in order words to treat finite systems and sources [4.40]. If we restrict ourselves to cylindrical symmetry, a complementary and also quite efficient tool can be found in the recently developed multipole expansion technique [4.41, 4.42]. Apart from the field pattern generated by a source, this approach allows one to calculate the local density of states (LDOS): For applications to quantum optical experiments in PCs it is necessary to investigate not only the (overall) availability of modes with frequency ω but also the local coupling strength of an emitter at a certain position $\boldsymbol{r}$ in the PC to the electromagnetic environment provided by the PC. Consequently, it is the overlap matrix element of the emitters dipole moment to the eigenmodes (Bloch functions) that is determining quantum optical properties such as decay rates etc. [4.25]. This may be combined into the local DOS (LDOS), $N(\boldsymbol{r}, \omega)$, which, for an infinite system, is defined as

$$N(\boldsymbol{r}, \omega) = \sum_n \int_{BZ} d^2k \; |E_{n\boldsymbol{k}}(\boldsymbol{r})|^2 \, \delta(\omega - \omega_n(\boldsymbol{k})). \tag{4.16}$$

Similar to the DOS, the LDOS of an infinite system vanishes for frequencies lying in the band gap, revealing the suppression of light emission at those frequencies. However, actual devices are not of infinite extent, and, therefore, in these finite-sized structures the LDOS will be very small but non vanishing. For finite systems, the LDOS can be obtained by extracting the imaginary part of Green's tensor $\mathcal{G}(\boldsymbol{r}, \boldsymbol{r}; \omega)$

$$N(\boldsymbol{r}; \omega) = -\frac{2\omega n_{Si}^2}{\pi c^2} \, \mathrm{Im}\mathrm{Tr}[\mathcal{G}(\boldsymbol{r}, \boldsymbol{r}; \omega)] \; , \tag{4.17}$$

where n_{Si} represents the index of refraction of the background where the air pores are embedded. The Green's tensor $\mathcal{G}(\boldsymbol{r}, \boldsymbol{r}_s; \omega)$ represents the field distribution at an observation point $\boldsymbol{r}$ generated by δ-source at $\boldsymbol{r}_s$. For infinite systems, it is straightforward to show that (4.17) agrees with (4.16). In the present case of a TM-polarized radiation in a 2D PC only the G_{zz} component of the Green's tensor is needed and satisfies the wave equation

$$\left(\partial_x^2 + \partial_y^2\right) G_{zz} + \frac{\omega^2}{c^2} \epsilon(\boldsymbol{r}) G_{zz} = \delta(\boldsymbol{r} - \boldsymbol{r}_s). \tag{4.18}$$

The multipole method consists in expanding Green's function G_{zz} in cylindrical harmonics both outside and inside the pores that comprise the PC. Subsequently the corresponding expansion coefficients are obtained by imposing appropriate continuity conditions across the pore surfaces and the Sommerfeld radiation condition as a boundary condition at infinity [4.41, 4.42]. In

particular, we consider a total of N_c pores embedded in a silicon background. Inside the l^{th} cylinder and in a coordinate system centered around the pore center $\boldsymbol{r}_l$, the G_{zz} is given by

$$G^{\text{int}}_{zz,l}(\boldsymbol{r},\boldsymbol{r}_s) = \frac{1}{4i}\chi^{\text{int}}_l(\boldsymbol{r}_s)H^{(1)}_0(kn_l|\boldsymbol{r}-\boldsymbol{r}_s|) + \sum_{m=-\infty}^{\infty} C^l_m J_m(kn_l|\boldsymbol{r}-\boldsymbol{r}_l|)\, e^{im\arg(\boldsymbol{r}-\boldsymbol{r}_l)}\ . \tag{4.19}$$

Here, $k = n_{Si}\omega/c$ is the wavenumber in the background material (silicon), $\boldsymbol{r}_l$ is the cylinder position, and the value of χ^{int}_l indicates whether $\boldsymbol{r}_s$ lies inside or outside of the l^{th} cylinder ($\chi^{\text{int}}_l = 1$ or $\chi^{\text{int}}_l = 0$, respectively). Finally, $\arg(\boldsymbol{r}-\boldsymbol{r}_l)$ denotes the polar angle of the vector $\boldsymbol{r}-\boldsymbol{r}_l$, and $H^{(1)}_0$ and J_m denote Hankel and Bessel functions, respectively. A similar expression for G_{zz} at an observation point $\boldsymbol{r}$ in proximity to but outside of pore q centered at $\boldsymbol{r}_q$ can be written as

$$G^{\text{ext}}_{zz}(\boldsymbol{r},\boldsymbol{r}_s) = \frac{1}{4i}\chi^{\text{ext}}(\boldsymbol{r}_s)H^{(1)}_0(k|\boldsymbol{r}-\boldsymbol{r}_s|) + \sum_{q=1}^{N_c}\sum_{m=-\infty}^{\infty} B^q_m H^{(1)}_m(k|\boldsymbol{r}-\boldsymbol{r}_s|)e^{im\arg(\boldsymbol{r}-\boldsymbol{r}_s)}\ . \tag{4.20}$$

Again χ^{ext} accounts for the position of the source.

The coefficients C^l_m of (4.19) and B^l_m in (4.20) for the same pore l are linked through continuity conditions across the pore surface. These continuity conditions together with the requirement of consistency of the various expansions centered around different pores give rise to the full multiple scattering problem and determine a system of linear equations. Once this system is solved, the Green's function $G^{\text{ext}}_{zz}(\boldsymbol{r},\boldsymbol{r}_s)$ can be reconstructed and field distributions and LDOS may be obtained (for details of the calculations as well as the implementation, we refer to [4.42]).

To demonstrate the feasibility of this approach as a modeling tool, we discuss a beamsplitter based on the optimized bend designed within the Wannier function approach (see Sect. 4.3.5). In Fig. 4.7 we display the field distribution of a plane wave (frequency $\omega = 0.282 \times 2\pi c/a$) impinging on a trial beamsplitter based on the naive beamsplitter (upper left in Fig. 4.6). Although the wave couples into the device through the input waveguide, this beamsplitter is unable to guide any radiation to any of the output ports and all the incoming radiation is reflected back. The failure of this naive example of a beamsplitter manifests the need of a more thorough investigation of the parameters to construct working devices. A more complicated beamsplitter based on the optimized bend design (lower right in Fig. 4.6) is depicted in Fig. 4.8. The good operation characteristics of the device for the same freqquncy ($\omega = 0.282 \times 2\pi c/a$) are apparent. More precisely, a analysis of the

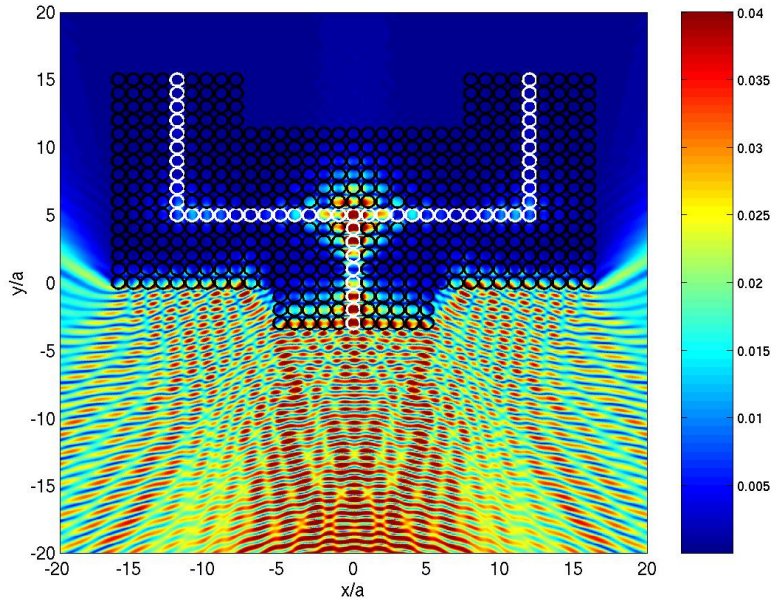

Fig. 4.7. Field distribution of a beamsplitter design based on the naive beamsplitter (upper left in Fig. 4.6). A point source far away from the PC structure emits at $\omega = 0.282 \times 2\pi c/a$, so that effectively a plane wave impinges on the PC structure. Clearly visible is the coupling into the central waveguide structure (Defect pores infilled with polymer are indicated through a white circle). Little intensity is transfered to the arms of the beamsplitter and practically nothing is transmitted around the bend. The parameters of the underlying PC are the same as those in Fig. 4.1.

Poynting vector in the input waveguide and the two output waveguides reveals that about 92% of the intensity are transmitted, 46% in each arm of the beamsplitter [4.43].

So far, we have been considering devices built within perfect lattices. This, unfortunately, is far from the experimental situation. Defects or imperfections are always present and they greatly influence the response of any actual device. It is thus important to characterize the effects of disorder on the device performance. As an illustration, we consider the optimized beamsplitter of Fig. 4.8 as the "perfect" device and suppose that during the fabrication process fabricational tolerances lead to a random variation of the pore diameter ranging from $r/a = 0.46$ to $r/a = 0.48$ (corresponding roughly to 3% radial disorder). The resulting performance for the operating frequency $\omega = 0.282 \times 2\pi c/a$ of the "perfect" device is depicted in Fig. 4.9. Clearly, the performance is compromised for even this moderate degree of disorder of about 3%. Although this speaks for itself, we would like to emphasize the im-

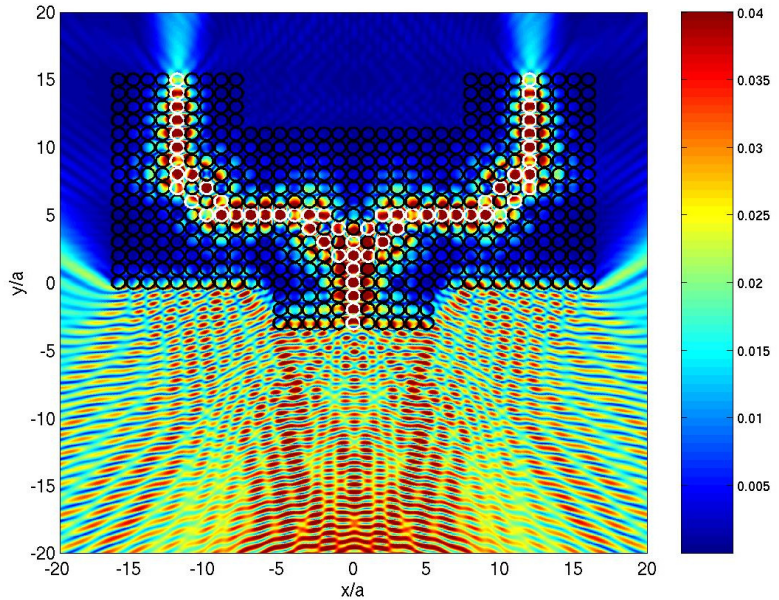

Fig. 4.8. Field distribution of a beamsplitter design based on the optimized beamsplitter (lower right in Fig. 4.6). A point source far away from the PC structure emits at $\omega = 0.282 \times 2\pi c/a$, so that effectively a plane wave impinges on the PC structure. Clearly visible is the coupling into the central waveguide structure (Defect pores infilled with polymer are indicated through a white circle). Substantial intensity is transfered to the arms of the beamsplitter and is fully transmitted around the bend, resulting in an effective beamsplitter. The parameters of the underlying PC are the same as those in Fig. 4.1.

portance of systematic investigations of the effects of fabricational tolerances on the performance of PC-based devices. This area of research has received very little attention until now.

4.5 Conclusions and Outlook

In summary, we have outlined a framework based on solid-state theoretical methods that allows one to qualitatively and quantitatively treat electromagnetic wave propagation in PCs. Photonic bandstructure computations for infinitely extended PCs provides photonic bandstructures and other physical quantities such as DOS and group velocities [4.26,4.27]. Furthermore, the input of bandstructure calculations facilitate the construction of maximally localized photonic Wannier functions which allow one to efficiently obtain the properties of defect structures embedded in PCs. In particular, the efficiency

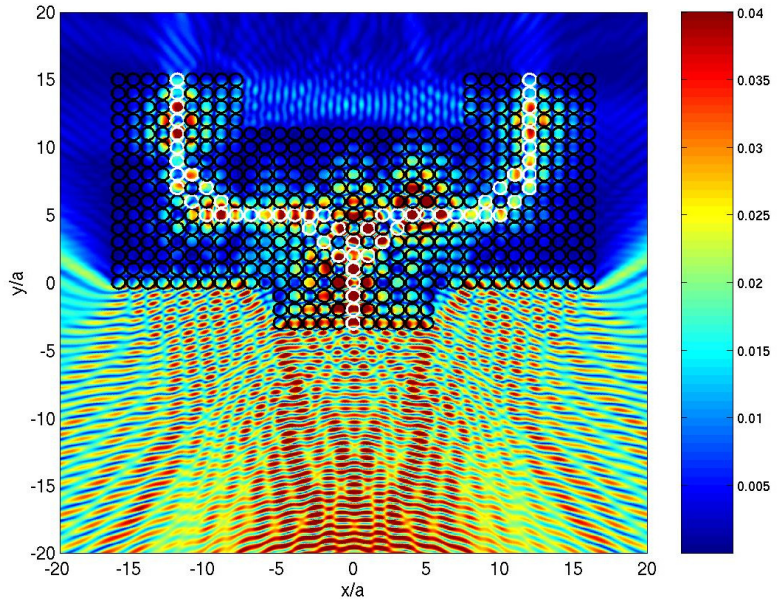

Fig. 4.9. Field distribution of a beamsplitter including fabricational tolerances. The beamsplitter is based on the optimized design of Fig. 4.8 and a random variation of the pore diameter ranging from $r/a = 0.46$ to $r/a = 0.48$ (roughly 3% radial disorder) has been added in order to model fabricational imperfections. A point source far away from the PC structure emits at $\omega = 0.282 \times 2\pi c/a$, so that effectively a plane wave impinges on the PC structure (Defect pores infilled with polymer are indicated through a white circle). The rather poor performance of the device is evident when comparing with the simulation for the perfect structure in Fig. 4.8. The parameters of the underlying PC are the same as those in Fig. 4.1.

of the Wannier function approach allows one to investigate large-scale PC circuits which, to date, are beyond the reach of standard simulation techniques such as FDTD or FE methods. Perhaps even more important is the fact that using the Wannier function approach facilitates the efficient exploration of huge parameter spaces for the design of defect structures embedded in a given PC basis structure.

The Wannier function approach is complemented by a multipole expansion technique which are well-suited for the investigation of finite-sized PCs. The usefulness of this multipole expansion manifests itself when we are considering efficient designs for actual finite-sized devices. A judicious approach that combines the results of optimizations via Wannier function studies with the multipole expansion technique has allowed us to desgin a realistic beamsplitter. Unfortunately, the experimental situation is far from ideal and the

lattice where the design is realized is not defect-free. We introduced realistic fabricational tolerances in into the optimized beamsplitter and analyzed its response. Under these conditions the device clearly lost its functionality, showing the importance of finding designs that are as robust as possible under the influence of fabricational imperfections.

Acknowledgments

This work was supported by the Center for Functional Nanostructures (CFN) of the Deutsche Forschungsgemeinschaft (DFG) within project A 1.2. The research of K.B. is further supported by the DFG under grant Bu 1107/2-2 (Emmy-Noether program). The work of M.S. is funded in the framework of the DFG Research Training Group 786 *Mixed Fields and Nonlinear Interactions* at the University of Karlsruhe.

References

[4.1] G.P. Agrawal: *Nonlinear Fiber Optics*, 3rd edn (Academic Press, San Diego Dan Francisco New York Boston London Sydney Tokyo 2001)
[4.2] R. März: *Integrated Optics: Design and Modeling*, (Artech House, 1995)
[4.3] E. Yablonovitch, Phys. Rev. Lett. **58**, 2059 (1987)
[4.4] Phys. Rev. Lett. **58**, 2486 (1987)
[4.5] A. Birner, R.B. Wehrspohn, U.M. Gösele, and K. Busch, Adv. Mater. **13**, 377 (2001)
[4.6] T.F. Krauss and R.M. de la Rue, Prog. Quantum Electron. **23**, 51 (1999)
[4.7] A. Forchel et al., Microelectron. Eng. **53**, 21 (2000)
[4.8] M. Loncar, T. Doll, J. Vuckovic, and A. Scherer, J. Lightwave Technol. **18**, 1402 (2000)
[4.9] H. Benisty et al., IEEE J. Quantum Electron. **38**, 770 (2002)
[4.10] S. Noda, M. Imada, A. Chutinan, and N. Yamamoto, Opt. Quantum Electron. **34**, 723 (2002)
[4.11] C. Liguda et al., Appl. Phys. Lett. **78**, 2434 (2001)
[4.12] A.C. Edrington et al., Adv. Mater. **13**, 421 (2001)
[4.13] A. Rosenberg, R.J. Tonucci, H.B. Lin, and E.L. Shirley, Phys. Rev. B **54**, R5195 (1996)
[4.14] O.J.A. Schueller et al., Appl. Opt. **38**, 5799 (1999)
[4.15] S.-Y. Lin et al., Nature **394**, 251 (1998)
[4.16] S. Noda, K. Tomoda, N. Yamamoto, and A. Chutinan, Science **289**, 604 (2000)
[4.17] J.E.G.J. Wijnhoven and W.L. Vos, Science **281**, 802 (1998)
[4.18] A. Blanco et al., Nature **405**, 437 (2000)
[4.19] Y.A. Vlasov, X.Z. Bo, J.C. Sturm, and D.J. Norris, Nature **414**, 289 (2001)
[4.20] M. Campbell et al., Nature **404**, 53 (2000)
[4.21] Y.V. Miklyaev et al., Appl. Phys. Lett. **82**, 1284 (2003)
[4.22] H.B. Sun, S. Matsuo, and H. Misawa, Appl. Phys. Lett. **74**, 786 (1999)
[4.23] H.B. Sun et al., Appl. Phys. Lett. **79**, 1 (2001)

[4.24] M. Straub and M. Gu, Opt. Lett. **27**, 1824 (2002)
[4.25] N. Vats, S. john, and K. Busch, Phys. Rev. A **65**, 043808 (2002)
[4.26] K. Busch and S. John, Phys. Rev. E **58**, 3896 (1998)
[4.27] D. Hermann, M. Frank, K. Busch, and P. Wölfle, Optics Express **8**, 167 (2001)
[4.28] K.-M. Ho, C.T. Chan, and C.M. Soukoulis Phys. Rev. Lett. **65**, 3152 (1990)
[4.29] K. Busch and S. John, Phys. Rev. Lett. **83**, 967 (1999)
[4.30] A. Brandt, S. McCormick, and J. Ruge, SIAM J. Sci. Stat. Comput. **4**, 244 (1983)
[4.31] K. Busch, S.F. Mingaleev, A. Garcia-Martin, M. Schillinger, D. Hermann, J. Phys.: Condens. Matter **15**, R1233 (2003)
[4.32] N. Marzari and D. Vanderbilt, Phys. Rev. B **56**, 12847 (1997)
[4.33] A. Garcia-Martin, D. Hermann, K. Busch, and P. Wölfle, Mater. Res. Soc. Symp. Proc. **722**, L 1.1 (2002)
[4.34] D.M. Whittaker and M.P. Croucher, Phys. Rev. B **67**, 085204 (2003)
[4.35] A. Mekis et al., Phys. Rev. Lett. **77**, 3787 (1996)
[4.36] J.D. Joannopoulos, P.R. Villeneuve, and S.H. Fan, Nature **386**, 143 (1997)
[4.37] S.F. Mingaleev and Y.S. Kivshar, Opt. Lett. **27**, 231 (2002)
[4.38] S.F. Mingaleev and K. Busch, Opt. Lett. **28**, 619 (2003)
[4.39] H. Brand: *Schaltungslehre linearer Mikrowellennetze*, (Hirzel, Stuttgart 1995)
[4.40] D. Hermann, A. Garcia-Martin, J.J. Saenz, S.F. Mingaleev, M. Schillinger, and K. Busch, in preparation
[4.41] A.A. Asatryan et al., Phys. Rev. E **63**, 046612 (2001)
[4.42] A.A. Asatryan et al., Waves in Random Media **13**, 9 (2003)
[4.43] F. Hagmann and K. Busch, unpublished